IOP Publishing and International Atomic Energy Agency Nuclear Fusion

Nucl. Fusion **53** (2013) 104005 (15pp) doi:10.1088/0029-5515/53/10/104005

An overview of KSTAR results

Jong-Gu Kwak[1], Y.K. Oh[1], H.L. Yang[1], K.R. Park[1], Y.S. Kim[1], W.C. Kim[1], J.Y. Kim[1], S.G. Lee[1], H.K. Na[1], M. Kwon[1], G.S. Lee[1], H.S. Ahn[1], J.-W. Ahn[10], Y.S. Bae[1], J.G. Bak[1], E.N. Bang[1], C.S. Chang[11], D.H. Chang[2], Z.Y. Chen[1], K.W. Cho[1], M.H. Cho[4], M. Choi[4], W. Choe[5], J.H. Choi[1], Y. Chu[1], K.S. Chung[6], P. Diamond[9], L. Delpech[21], H.J. Do[1], N. Eidietis[12], A.C. England[10], R. Ellis[11], T. Evans[12], G. Choe[4], L. Grisham[11], Y. Gorelov[12], H.S. Hahn[1], S.H. Hahn[1], W.S. Han[1], T. Hatae[15], D. Hillis[10], T. Hoang[21], J.S. Hong[1], S.H. Hong[1], S.R. Hong[1], J. Hosea[11], D. Humphreys[12], Y.S. Hwang[3], A. Hyatt[12], K. Ida[16], Y.K. In[14], S. Ide[15], Y.B. Jang[1], Y.M. Jeon[1], J.I. Jeong[1], N.Y. Jeong[1], S.H. Jeong[2], J.K. Jin[1], M. Joung[1], J. Ju[1], K. Kawahata[16], C.H. Kim[1], Hee-Su Kim[1], H.S. Kim[3], H.J. Kim[1], H.K. Kim[1], H.T. Kim[1], J.H. Kim[1], J. Kim[1], J.C. Kim[1], Jong-Su Kim[1], Jung-Su Kim[1], J.H. Kim[4], Kyung-Min Kim[1], K.J. Kim[3], K.P. Kim[1], M.K. Kim[1], S.T. Kim[1], S.W. Kim[1], Y.J. Kim[1], Y.K. Kim[6], Y.O. Kim[1], J.S. Ko[1], W.H. Ko[1], Y. Kogi[17], E. Kolemen[11], J.D. Kong[1], S.W. Kwak[1], J.M. Kwon[1], O.J. Kwon[7], D.G. Lee[1], D.R. Lee[1], D.S. Lee[1], H.J. Lee[1], J. Lee[4], J.H. Lee[1], K.D. Lee[1], K.S. Lee[1], S.H. Lee[5], S.I. Lee[1], S.M. Lee[1], T.G. Lee[1], W. Lee[4], W.L. Lee[1], D.S. Lim[1], X. Litaudon[21], J. Lohr[12], D. Mueller[11], K.M. Moon[1], D.H. Na[3], Y.S. Na[3], Y.U. Nam[1], W. Namkung[4], K. Narihara[16], S.T. Oh[1], D.G. Oh[1], T. Ono[15], B.H. Park[1], D.S. Park[1], G.Y. Park[1], H. Park[4], H.T. Park[1], J.K. Park[11], J.S. Park[1], M.K. Park[1], S.H. Park[1], S. Park[1], Y.M. Park[1], Y.S. Park[13], R. Parker[22], D.R. Rhee[1], S.A. Sabbagh[13], K. Sakamoto[15], S. Shiraiwa[22], D.C. Seo[1], S.H. Seo[1], J.C. Seol[1], Y.J. Shi[1], S.H. Son[1], N.H. Song[1], T. Suzuki[15], L. Terzolo[1], M. Walker[12], G. Wallace[22], K. Watanabe[15], S.J. Wang[1], H.J. Woo[6], I.S. Woo[1], M. Yagi[18], Y.W. Yu[19], I. Yamada[16], Y. Yonekawa[1], C.M. Yoo[4], K.I. You[1], J.W. Yoo[1], G.S. Yun[4], M.G. Yu[3], S.W. Yoon[1], W. Xiao[20], S. Zoletnik[23] and the KSTAR Team[1]

[1] National Fusion Research Institute, Daejeon 305-333, Korea
[2] Korea Atomic Energy Research Institute, Daejeon, Korea
[3] Seoul National University, Seoul, Korea
[4] Pohang University of Science and Technology, Pohang, Korea
[5] Korea Advanced Institute of Science and Technology, Daejeon, Korea
[6] Hanyang University, Seoul, Korea
[7] Daegu University, Daegu, Korea
[8] Ajou University, Sawon, Kyonggi, Korea
[9] University of San Diego, San Diego, CA, USA
[10] Oak Ridge National Laboratory, Oak Ridge, TN, USA
[11] Princeton Plasma Physics Laboratory, Princeton, NJ, USA
[12] General Atomics, San Diego, CA, USA
[13] Columbia University, New York, NY, USA
[14] Fartech, San Diego, CA, USA
[15] Japan Atomic Energy Agency, Naka, Ibaraki, Japan
[16] National Institute of Fusion Science, Toki, Gifu, Japan
[17] Fukuoka Institute of Technology, Fukuoka, Japan
[18] Kyushu University, Fukuoka, Japan
[19] Institute of Plasma Physics of Academia Sinica, Hefei, Anhui, People's Republic of China
[20] Southwestern Institute of Physics, Chengdu, People's Republic of China
[21] CEA-IFRM, France
[22] Massachusetts Institute of Technology, USA
[23] Wigner RCP, EURATOM Association HAS, Budapest, Hungary

E-mail: jgkwak@nfri.re.kr

Received 5 December 2012, accepted for publication 15 April 2013
Published 26 September 2013
Online at stacks.iop.org/NF/53/104005

Abstract
Since the first H-mode discharges in 2010, the duration of the H-mode state has been extended and a significantly wider operational window of plasma parameters has been attained. Using a second neutral beam (NB) source and improved tuning of equilibrium configuration with real-time plasma control, a stored energy of $W_{\rm tot} \sim 450$ kJ has been achieved with a corresponding energy confinement time of $\tau_E \sim 163$ ms. Recent discharges, produced in the fall of 2012, have reached plasma $\beta_{\rm N}$ up to 2.9 and surpassed the $n = 1$ ideal no-wall stability limit computed for H-mode pressure profiles, which is one of the key threshold parameters defining advanced tokamak operation. Typical H-mode discharges were operated with a plasma current of 600 kA at a toroidal magnetic field $B_{\rm T} = 2$ T. L–H transitions were obtained with 0.8–3.0 MW of NB injection power in both single- and double-null configurations, with H-mode durations up to ~15 s at 600 kA of plasma current. The measured power threshold as a function of line-averaged density showed a roll-over with a minimum value of ~0.8 MW at $\bar{n}_{\rm e} \sim 2 \times 10^{19}$ m^{-3}. Several edge-localized mode (ELM) control techniques during H-mode were examined with successful results including resonant magnetic perturbation, supersonic molecular beam injection (SMBI), vertical jogging and electron cyclotron current drive injection into the pedestal region. We observed various ELM responses, i.e. suppression or mitigation, depending on the relative phase of in-vessel control coil currents. In particular, with the 90° phase of the $n = 1$ RMP as the most resonant configuration, a complete suppression of type-I ELMs was demonstrated. In addition, fast vertical jogging of the plasma column was also observed to be effective in ELM pace-making. SMBI-mitigated ELMs, a state of mitigated ELMs, were sustained for a few tens of ELM periods. A simple cellular automata ('sand-pile') model predicted that shallow deposition near the pedestal foot induced small-sized high-frequency ELMs, leading to the mitigation of large ELMs. In addition to the ELM control experiments, various physics topics were explored focusing on ITER-relevant physics issues such as the alteration of toroidal rotation caused by both electron cyclotron resonance heating (ECRH) and externally applied 3D fields, and the observed rotation drop by ECRH in NB-heated plasmas was investigated in terms of either a reversal of the turbulence-driven residual stress due to the transition of ion temperature gradient to trapped electron mode turbulence or neoclassical toroidal viscosity (NTV) torque by the internal kink mode. The suppression of runaway electrons using massive gas injection of deuterium showed that runaway electrons were avoided only below 3 T in KSTAR. Operation in 2013 is expected to routinely exceed the $n = 1$ ideal MHD no-wall stability boundary in the long-pulse H-mode ($\geqslant$10 s) by applying real-time shaping control, enabling $n = 1$ resistive wall mode active control studies. In addition, intensive works for ELM mitigation, ELM dynamics, toroidal rotation changes by both ECRH and NTV variations, have begun in the present campaign, and will be investigated in more detail with profile measurements of different physical quantities by techniques such as electron cyclotron emission imaging, charge exchange spectroscopy, Thomson scattering and beam emission spectroscopy diagnostics.

(Some figures may appear in colour only in the online journal)

1. Introduction

KSTAR is a long-pulse superconducting tokamak aiming to explore high-beta operation and is expected to play an important role in providing the extrapolation to ITER and K-DEMO [1]. Since its first H-mode in 2010 (<2 s), the H-mode was more stably sustained in 2011 for longer durations up to about 5 s with similar values of plasma current and toroidal field as in the previous campaign, i.e. 0.6 MA and 1.6–2.0 T, respectively [2]. The duration of H-mode was extended to 15 s at 0.6 MA in the 2012 campaign with better control of the midplane gaps, which was found to be critical for H-mode sustainment in the previous campaign. In L-mode plasmas, 1 MA plasma current was achieved, and a pulse length longer than 12 s was sustained in L-mode at 0.6 MA.

The extended operating space described in stability-relevant parameters of internal inductance $l_{\rm i}$, and normalized beta $\beta_{\rm N}$ is shown in figure 1. Compared with the first H-mode with maximum $\beta_{\rm N} = 1.3$, $W_{\rm tot} = 258$ kJ and $\tau_E = 148$ ms [3], operating parameters reached higher values, $\beta_{\rm N} = 1.9$, $W_{\rm tot} = 340$ kJ with a corresponding $\tau_E = 171$ ms, in 2011. The plasma internal inductance was also reduced to 0.94 from 1.15 at the maximum $\beta_{\rm N}$. The equilibrium enhancement towards higher values of $\beta_{\rm N}/l_{\rm i} > 2$ in 2011 without a substantial increase in the auxiliary heating power from 2010 is significant. Enhanced energy confinement due to improved wall conditioning by boronization and higher bake out temperature (increasing from 200 °C up to 260 °C on the carbon tile surface) has allowed this improvement. Recently, in the fall of 2012, a substantial increase in $\beta_{\rm N}$ and $\beta_{\rm N}/l_{\rm i}$ was observed, and discharges have reached and surpassed the computed $n = 1$ ideal no-wall stability limit computed for H-mode pressure profiles, a key threshold defining advanced tokamak operation. The ideal MHD stability code DCON computes the $n = 1$ no-wall boundary to be most closely positioned to the 2011 database at $\beta_{\rm N} = 2.5$, $l_{\rm i} = 0.7$. These no-wall limit calculations utilize equilibria with H-mode pressure profiles and standard q profile shapes with minimum q values varying from greater than unity, to less than 2. This approach yields the most reliable computation of the $n = 1$ no-wall limit as a function of ($l_{\rm i}$, $\beta_{\rm N}$) until internal pitch angle measurements become routinely available

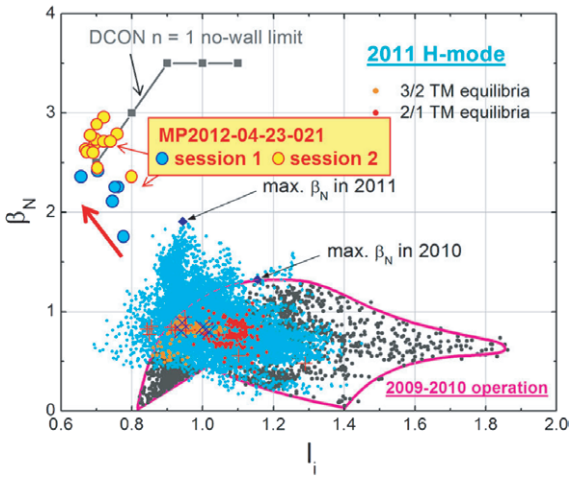

Figure 1. KSTAR equilibrium operating space from the 2012 campaign and prior discharges. About 16 000 equilibria from 137 shots (93 shots from 2011) and 20 shots from 2012 are shown. Expansion of the operating space in l_i and β_N is illustrated, along with points describing the presence of 3/2 (orange points) and 2/1 tearing modes (red points). The blue crosses indicate the 3/2 mode onset time, and the red plus symbols indicate the 2/1 mode onset time.

on KSTAR. Full details of the no-wall limit calculations and their dependence on l_i are given in [4]. The plasma β_N has reached 2.9 transiently, sustained $\beta_N \sim 2.8$ for more than 1 s, and fluctuated above $\beta_N = 2.5$ for programmed pulse lengths of 6 s. Maximum β_N values are plotted in figure 1. Plasmas were in the range $0.65 < l_i < 0.8$, and β_N/l_i exceeded 4—a 100% increase over plasmas from 2011. A newly available second neutral beam injection (NBI) source was used in these experiments, doubling the input power to 3 MW versus past experiments. These experiments were conducted in plasmas with $1.3 < B_T < 1$ with maximum β_N reached at B_T of 1.3–1.4 T. Analysis continues on these recent data, but at present, these plasmas appear to be either confinement-limited, or limited by impurity accumulation, rather than a disruption limit caused by a growing global kink/ballooning mode. The impurity accumulation is not a specific characteristic of these plasmas. It should be noted that the ideal $n = 1$ no-wall limit is not expected to be the marginal stability point for kink/ballooning, or resistive wall modes (RWMs), as kinetic stabilization effects in a rotating plasma allow stabilization of these modes above this limit [5–7]. By successfully solving past iso-flux control issues, sustained elongation higher than the designed target value of 2 was achieved in many equilibria spanning $0.7 < l_i < 1.1$. Figure 1 also shows the onset (l_i, β_N) for 2/1 and 3/2 tearing modes, and the broad range over which these modes exist. Details of MHD modes observed in the extended operation space are discussed in section 6 and in [8]. L–H transitions were obtained with 0.8–3.0 MW of P_{NBI} in the double-null (DN) configuration. The measured L–H power threshold as a function of density shows a roll-over with a minimum value of ~0.8 MW at $\bar{n}_e \sim 2 \times 10^{19}$ m^{-3}, which shows a clear deviation from the prediction of present multi-machine scaling laws. Various methods of edge-localized mode (ELM) control have been implemented and tested during H-mode including resonant magnetic perturbation (RMP), supersonic molecular beam injection (SMBI), vertical jogging

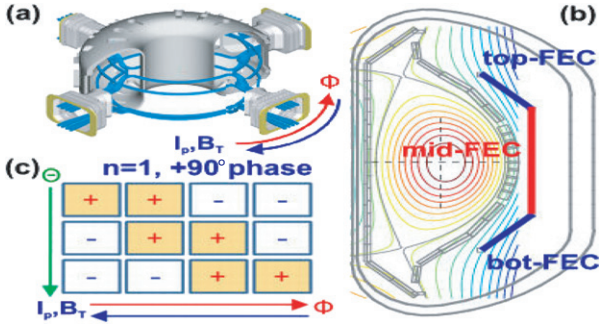

Figure 2. Configurations of the KSTAR IVCC system. (*a*) 3D view of IVCC coils, (*b*) 2D view of three rows of IVCC, and (*c*) a schematic diagram of $n = 1$ RMP with +90° of phase among three rows of IVCC.

and electron cyclotron current drive (ECCD) injection inside the pedestal region. First, by using in-vessel control coil (IVCC), as shown in figure 2, we observed various ELM-RMP responses, i.e. suppression and mitigation, depending on the relative toroidal phase among its three rows of coils. During the ELM suppression experiments with the $n = 1, 90°$ phase RMP as the most resonant, ELMs were initially intensified with a reduction in frequency before being completely suppressed at a later stage. Although the $n = 1$ mode has a significantly higher possibility of mode locking compared with higher toroidal mode numbers, it substantially reduces the engineering needs by providing an easier path to ELM suppression for ITER and DEMO if an acceptable operation window can be found. Second, ELM pace-making by fast vertical jogging of the plasma column was demonstrated. ELM bursts were locked to 50 Hz vertical jogs with high reliability. With 25 mm of vertical jogging at 50 Hz utilizing the fast IVC coils, ELMs were triggered when the plasma moved away from the lower x-point with its maximum speed and this is consistent with the previous results reported by the TCV team [9]. Third, a newly installed SMBI system was also utilized for ELM control and a state of mitigated ELMs for a few tens of ELM periods was sustained by the optimized repetitive SMBI pulses. A simple cellular automata (sand-pile) model predicts that shallow deposition of SMBI near the pedestal foot induces small-scale high-frequency transport events, which prevent the pressure profile from building-up to marginality throughout the pedestal, thus avoiding large-scale ELMs. In addition, various physics topics were explored focusing on ITER-relevant physics issues such as intrinsic rotation driven by RF power injection and external 3D fields, runaway electron mitigation, MHD activities related to tearing mode (TM) and neoclassical toroidal viscosity (NTV), wall conditioning using ion cyclotron range of frequencies (ICRF) and electron cyclotron heating (ECH), and flux saving using ECH injection during the ramping period of the plasma current. A significant drop in toroidal rotation was measured during the central ECH in neutral beam (NB)-heated H-mode plasmas while the electron temperature and stored energy were increased. The underlying physical mechanisms are under investigation to explain the observed behaviour of toroidal rotation in terms of either a reversal of the turbulence-driven residual stress due to the transition of ion temperature gradient (ITG) to trapped electron mode (TEM) turbulence or NTV torque by the internal kink mode excited by ECH.

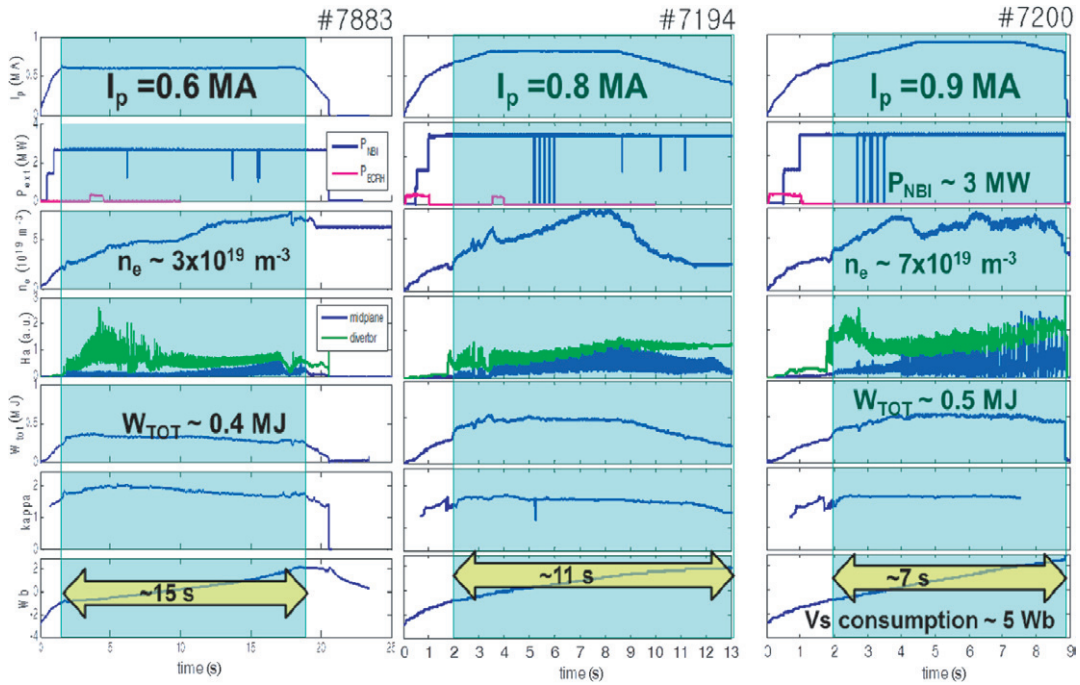

Figure 3. Extension of H-mode pulse length during the flat top to 15 s, 6 s, 3.5 s for (*a*) 0.6 MA, (*b*) 0.8 MA, and (*c*) 0.9 MA. NBI power is about 3 MW.

In summary, through the campaigns of the last two years after FEC 2010, an update of machine performance and key plasma experimental results will be described with respect to achievement from the plasma performance, ELM mitigation experiments using unique IVCCs and 2D electron cyclotron emission imaging (ECE-I) measurements, and toroidal rotation changes by electron cyclotron resonance heating (ECRH) and 3D field effects. In addition, the next five-year plan will be introduced in terms of heating power upgrade and key research topics.

2. Extending H-mode pulse duration at a high plasma current

By properly controlling the plasma shape and particle control, the pulse length of the H-mode at the flattop was extended to 15 s, 6 s and 3.5 s at 0.6 MA, 0.8 MA and 0.9 MA of plasma current, respectively, as shown in figure 3, whereas the duration of the H-mode was extended to 7 s at 0.8 MA including the ramping period. The pulse length is not limited by machine capabilities but by reactive power limitation of the grid power. Considering that the total ohmic flux capability of KSTAR is about 12 Wb and just only 5 Wb is consumed, it is conjectured that KSTAR has a capability of longer pulse of 20 s at 1 MA in inductive discharges with the present heating power. In addition, it is expected that particle control using the in-vessel cryo-pump and ECH would warranty stable long-pulse operation at high confinement mode.

3. Improvements of the diagnostic system

Diagnostic systems have been improved since 2010. The Thomson scattering diagnostic finally succeeded in producing the preliminary results by increasing the signal-to-noise level

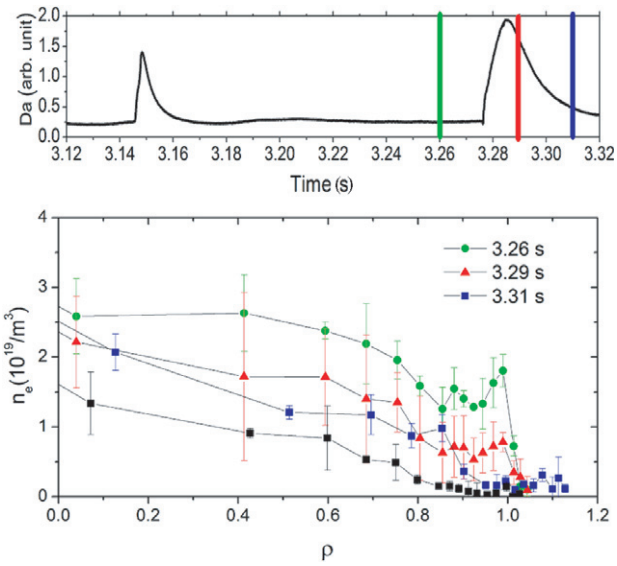

Figure 4. Measured density profile by the Thomson scattering system. The black line is the L-mode and the colour lines are the H-mode. The position of the pedestal top is located around $\rho = 0.95$.

through proper adjustment of voltage on the polychrometers. Due to the high repetition rate of 100 Hz of the laser source, it provides the time evolution of the pedestal behaviour of the H-mode between ELMs, as shown in figure 4. The Q band (33–50 GHz) and V band (50–75 GHz) reflectometers were also used to measure the electron density profile and they can measure the electron density up to 2.5×10^{19} m^{-3} when the toroidal magnetic field is 2 T. A typical time resolution is 35 μs and it is observed that the electron density is pumped out rapidly in about 0.2 ms, and it recovers slowly in about

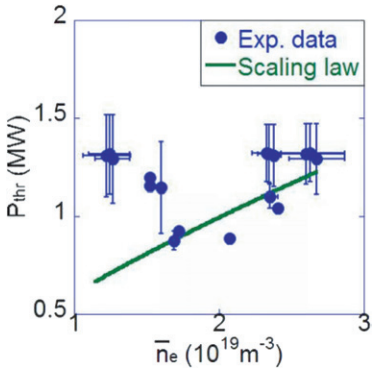

Figure 5. Measured L–H power threshold (P_{thr}) obtained during the experimental campaigns in 2011 (blue). Green line indicates the predicted P_{thr} from the multi-machine scaling law [11] and P_{thr} is the minimum of the loss power at the L–H transition.

10 ms for small ELMs and 50 ms for large ELMs, respectively. The ECE-I was used for identification of the ELM structure and the study of ELM suppression physics. Another ECE-I system has recently been installed at a toroidally different location and provided 3D images of ELMs and other MHD instabilities [10].

4. General characteristics of H-mode plasmas

Several H-mode characteristics were investigated such as the L–H power threshold, characteristics of ELMs and confinement, and the inter-ELM pedestal profile evolution. The L–H power threshold study reveals a roll-over of P_{thr} with minimum at $\bar{n}_e \sim 2\times10^{19}$ m^{-3}, as shown in figure 5. However, for $\bar{n}_e$ above 2×10^{19} m^{-3}, the evaluated P_{thr} agrees well with the prediction from the multi-machine scaling laws [11]. An analysis of $H_{89\text{-p}}$ indicates that the energy confinement is enhanced for most of the KSTAR H-modes as observed in other devices, $H_{89\text{-p}} \sim 1.6$–2.2. An interpretative simulation carried out using the ASTRA transport code reveals $H_{98(y,2)}$ of ~1.0 and a bootstrap current fraction of 25% representing typical H-mode plasmas [12]. The charge exchange spectroscopy (CES) measurement provided detailed structures of the T_i and V_ϕ pedestals and their evolutions during L $\rightarrow$ H and H $\rightarrow$ L transitions. The measured pedestal profiles revealed that the width of the V_ϕ pedestal is broader than that of T_i, as shown in figure 6. As the residual turbulence in the H-mode is expected to drive quite modest levels of turbulence and the neoclassical transport theory indicates $\chi_{i,neo} \gg \chi_{\phi,neo}$, we usually anticipate that the ion heat transport is higher than the momentum transport and, therefore, the ITG is steeper than the rotation gradient. In figure 7, we observe a strong linear correlation between ∇T_i and ∇V_ϕ during the transitions. This suggests that a single transport process controls both channels during the transitions and that the correlation of the gradients of quantities is more fundamental than the correlation of the quantities themselves. A detailed analysis of transport and micro-instabilities is in progress with the measured profiles.

KSTAR also showed three distinctive types of ELMy H-modes [11]: large type-I ELMs with low frequency and good confinement ($H_{98(y,2)} \sim 0.9$–1); intermediate ELMs with higher frequency and poorer confinement ($H_{98(y,2)} \sim 0.7$); mixed ELMs with large and small ELM peaks and good

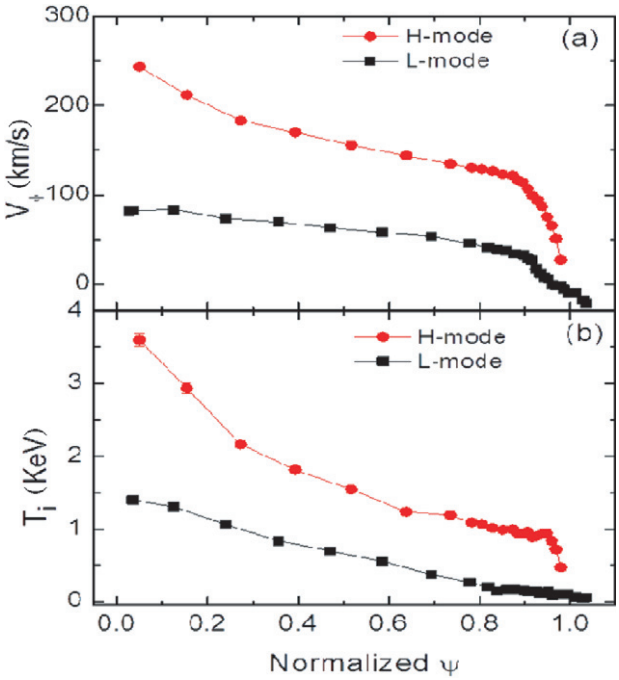

Figure 6. V_ϕ and T_i profiles measured by CES.

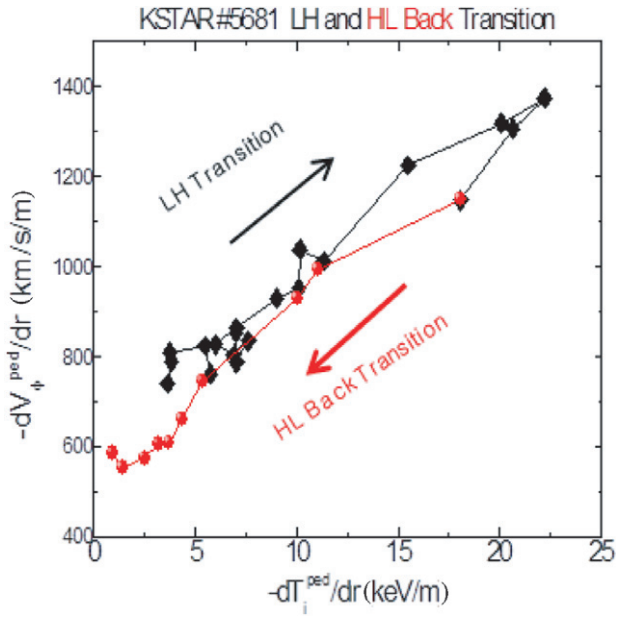

Figure 7. Correlation between pedestal ∇V_ϕ and ∇T_i during L $\rightarrow$ H transition (black dots) and H $\rightarrow$ L back transition (red dots).

confinement ($H_{98(y,2)} \sim 0.9$–1). Preliminary power scan data showed that the frequency of large type-I ELM and mixed ELM regimes increases with heating power, a typical feature of type-I ELMs. The ELM size of intermediate ELMs is not correlated with either the ELM frequency or the Greenwald density fraction, while it inversely depends on both quantities for type-I ELMs. Also, a wavelet analysis of Mirnov signals revealed that there is a long-lasting (20–50 ms) ELM precursor-like increased fluctuation level for type-I ELMs in the low-frequency band (25–50 kHz) before the ELM burst. However, the intermediate ELMy H-mode does not show precursor-like

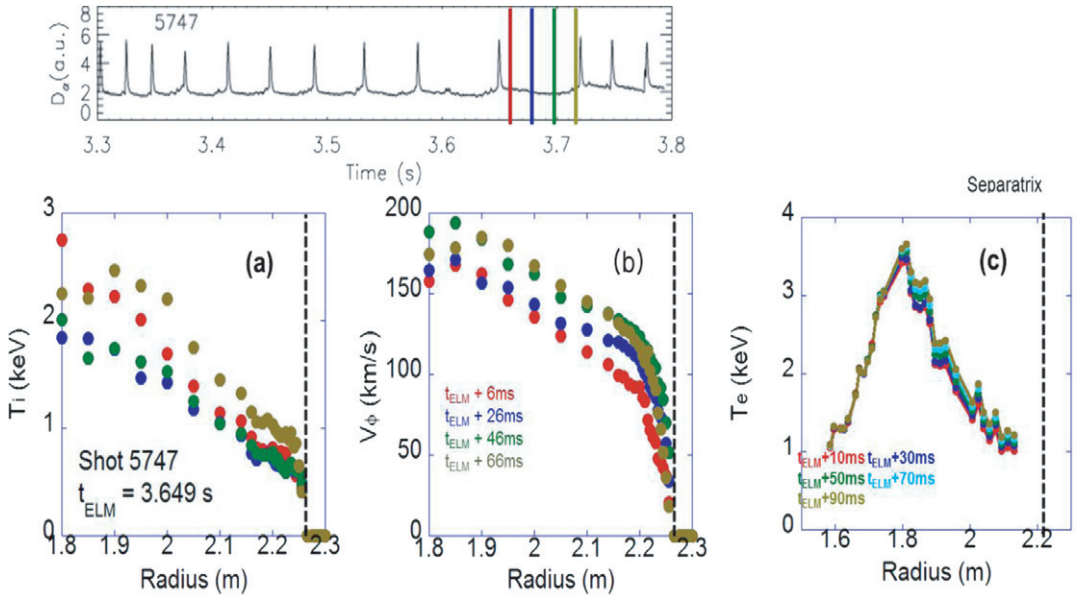

Figure 8. Inter-ELM profile evolution of (*a*) ion temperature (T_i), (*b*) V_ϕ, and (*c*) T_e. The data were taken at four time points between the ELMs. Plots (*a*) and (*b*) are for the same points for shot #5747 (colour coded in Dα time trace above). Plot (*c*) was taken for five inter-ELM time points for another shot [11].

signals but the broadband fluctuation level generally increases for the inter-ELM period compared with the type-I ELMy H-mode. Based on this difference in the magnetic signals as well as the ELM size and frequency characteristics and lower confinement quality than those for type-I ELMs, we suspect that the intermediate ELMs might be type-III ELMs. Profile measurements during an ELM cycle indicate that the T_i pedestal only jumps at the last stage (after 70–80% of the ELM cycle, see figure 8) whereas the T_e and V_ϕ pedestals steadily rise over the entire ELM cycle. This suggests that the contribution of ion pressure to the total pressure gradient that is necessary to cross the ELM stability boundary primarily comes in the last stage of the ELM cycle at KSTAR.

5. ELM mitigation experiments

One of the urgent issues for ITER is to control the ELMs to meet the material requirements on the divertor. Several methods have been used such as RMP, SMBI injection, plasma vertical jogging/kicking and edge-localized current drive by ECCD [13–15]. In particular, the application of RMPs using IVCC, which are intrinsic tools in KSTAR and can provide $n = 1$ and $n = 2$ types of non-axisymmetric magnetic perturbations via three rows of coils, has shown a substantial effect on ELM dynamics. First of all, the ELMs were completely suppressed by applying $n = 1$ RMP with +90° phases, which is the most resonant configuration to the $I_p = 0.6$ MA D-shaped plasma at $B_T = 2$ T [16]. The plasma exhibits two distinctive stages during the application of the RMP; an ELM intensification and an ELM suppression stage. As shown in figure 9, initially the electron density, stored energy and toroidal rotation were reduced by less than 10%. Then as ELMs were suppressed, they became stationary except for a gradual increase in electron density. Details of ELM dynamics in ELM-suppressed RMP discharges were observed from an electron cyclotron emission imaging (ECE-I) diagnostics, as

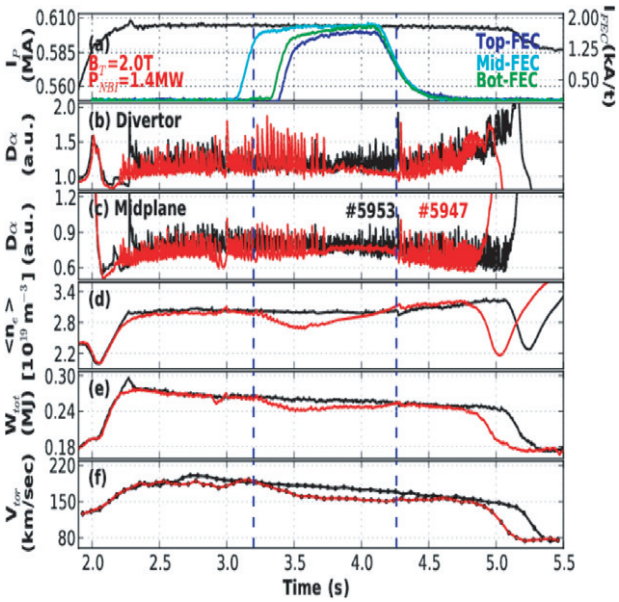

Figure 9. Comparison of ELM-suppressed RMP discharge (#5947) with a reference ELMy discharge (#5953). The applied three rows of RMP currents are indicated as top-, mid- and bot-FEC.

shown in figure 10. During the ELM intensification period (2 around 3.62 s), the spacing between the modes was enlarged and then the mode structure showed the chaotic state in the ELM mitigated state (3 around 4.31 s).

The superiority of the +90° phasing can be assessed by its efficiency on the edge versus core coupling of the perturbation. Since the coupling to the edge would be essential for pedestal modification while the coupling to the core would be unnecessary, we compared the NTV torque [17] by each phase when each Chirikov overlap width in the edge becomes as large as 15% in terms of the normalized poloidal flux [18]. This

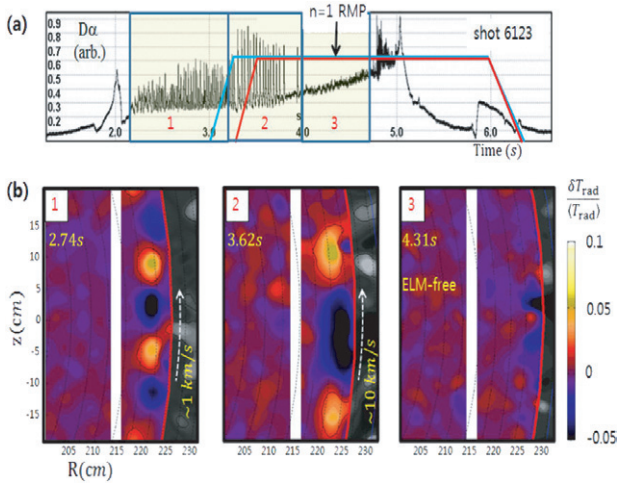

Figure 10. Time evolution of Dα (*a*) and the corresponding ECE-I picture around the pedestal (*b*).

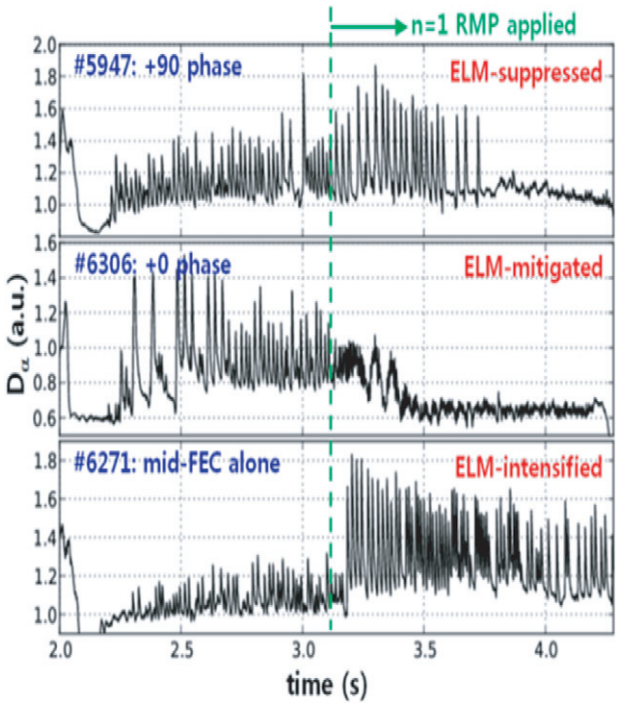

Figure 11. Various ELM responses to applied $n = 1$ RMPs. ELMs can be suppressed, mitigated or even intensified.

quantification can provide a useful guidance in the magnetic field optimization, based on a mixture of different hypotheses assuming stochastic transport for the edge and neoclassical transport for the core, although the scientific validity of such hypotheses is still under investigation. Analysis showed that the +90° phase indeed produces the minimal NTV torque, smaller by an order of magnitude compared with other phases, as is consistent with its unique demonstration on ELM suppression. In addition, our RMP experiments also observed that the $n = 1$ RMP with 0° phase, which is worth comparing with the JET $n = 1$ RMP provided by external coils [19], showed a possible mitigation of ELMs, as illustrated in figure 10. On the other hand, the mid-plane (mid-FEC) coil alone with $n = 1$ configuration, which corresponds to a similar but poloidally narrower magnetic perturbation than that of the 0° phase, showed that the ELMs can even be intensified. KSTAR will explore these various RMP effects on ELMs further in the next campaign to achieve a more comprehensive understanding of RMP physics.

Second, a newly installed SMBI system was also utilized for ELM control and a state of mitigated ELMs for a few tens of ELM periods was sustained by the optimized repetitive SMBI pulses. We observed an ELM frequency increase and an ELM amplitude decrease for a finite duration period after SMBI. Not only is an increase in frequency of $f_{\mathrm{ELMSMBI}}/f_{\mathrm{ELM0}} \sim$ 2–3.5 observed, but the ELM amplitude also decreases for several hundred milliseconds and the change in energy loss per ELM with SMBI compared with the phase without SMBI is almost decreased by 3%. The SMBI influence time (τI) is about 400 ms. During ELM mitigation, about 8% of the stored energy is lost, so confinement degradation is small. The core toroidal rotation (by XICS) is also observed to drop from ~140 km s^{-1} to ~130 km s^{-1} during τI and then slowly recovers to ~138 km s^{-1}. It is also observed that with SMBI, the low-frequency ($f < 10$ kHz, left-hand side of the shaded region) component of the edge particle flux spectrum in figure 12 decreases. The changes in the edge particle flux suggest that ELM mitigation is correlated with a decrease in lower frequency fluctuations and transport events in the pedestal. These inhibit the occurrence of large transport events, which span the entire pedestal width, and so mitigate ELMs [20]. The spectrum of edge density fluctuations was measured by beam emission spectroscopy (BES) [21]. In figure 13(*a*), after SMBI, the ELM frequency increases from 28 to 68 Hz and the ELM amplitude drops by more than half. The value of τ_I is about 400 ms. In (*b*) and (*c*), the blue curve shows the result without SMBI and the red curve is the analysis with SMBI. The corresponding time windows of the data are marked with blue and red bars in figure 13(*a*), respectively. The fluctuation intensity is measured by BES channel 3 at $R = 2.248$ m in figure 13(*b*), close to the pedestal top, from the outside direction. In figure 13(*c*), those are measured by BES channel 6 at $R = 2.277$ m, almost at the foot of the pedestal $R_{\mathrm{LCFS}} = 2.278$ m, by EFIT. There is no distinct difference shown in the density fluctuations (*b*) as compared with (*c*) in this figure. This means the particle source from SMBI has shallow penetration and SMBI does not reach the top of the pedestal [20, 22]. The obvious difference in the edge density fluctuation spectrum is that the low-frequency content drops, while the higher frequency content increases, as shown in figure 13(*c*) by the red curve. This is consistent with the idea that SMBI inhibits the formation of large avalanches or transport events, while triggering more small avalanches [23–25].

Third, ELM pace-making by fast vertical jogging of the plasma column was demonstrated. ELM bursts were locked to 50 Hz vertical jogs with high reliability. With 25 mm of vertical jogging at 50 Hz utilizing the fast IVC coils, ELMs were triggered when the plasma moved away from the lower x-point with its maximum speed, and this is consistent with the previously reported results by the TCV team. The multiple ELMs were triggered when the vertical excursion was further increased up to 75 mm. With this large jogging amplitude,

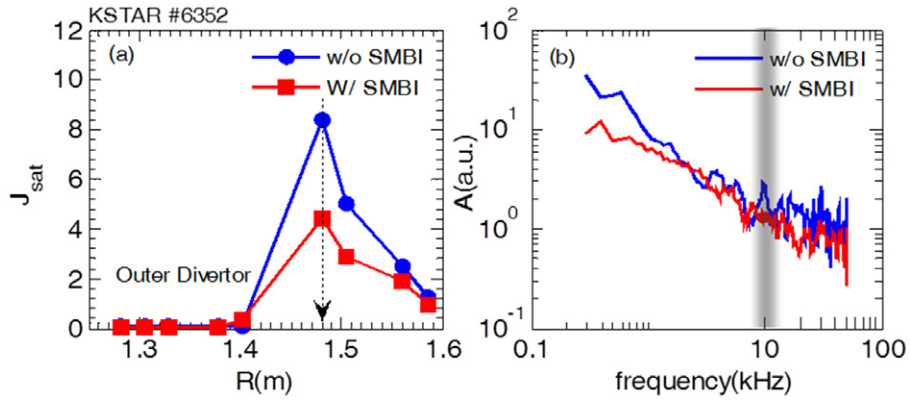

Figure 12. Frame (*a*) shows the measurement results from Langmuir probes at the outer divertor with and without SMBI for shot #6352. Frame (*b*) shows the spectrum analysis of J_{sat}.

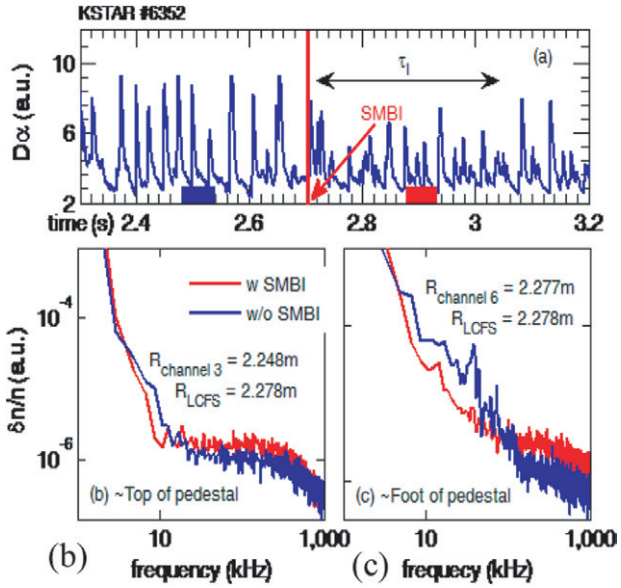

Figure 13. Comparison of the density fluctuation by BES at different positions in the pedestal region. (*a*) is the history of the D_a ELM monitor for shot 6352. SMBI was injected at 2.7 s. (*b*) and (*c*) are the spectrum of edge density fluctuations. The red and blue curves are with and without SMBI, respectively.

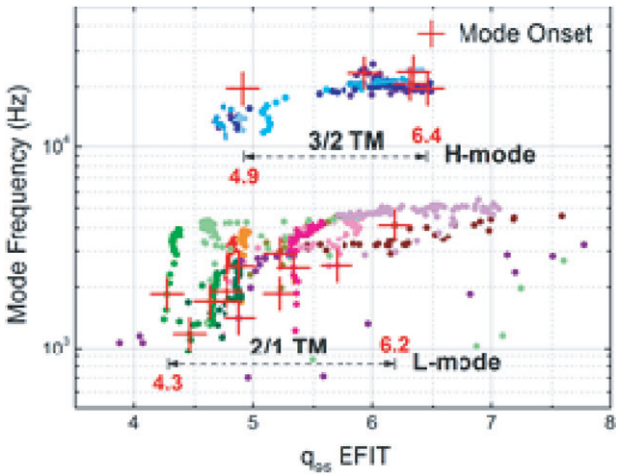

Figure 14. Mode frequency versus equilibrium q_{95} in 3/2 and 2/1 tearing mode evolutions. The evolution of each shot is shown by points of the same colour, and the values at the initial mode saturation are indicated by plus symbols.

the ELM triggering was observed only at the lower single null configuration.

6. MHD experiments

Rotating MHD modes are observed with perturbations having tearing rather than ideal parity, as determined by Mirnov and ECE [26] measurements. Modes with $m/n = 3/2$ (m structure by 2D ECE-I [27]) have an onset at lower l_i than modes with $m/n = 2/1$ in the range $0.5 < \beta_N < 1$, as shown in the expanded operating space in figure 1. The 3/2 modes are triggered during the H-mode phase but are relatively weak and do not substantially reduce W_{tot}. In contrast and surprisingly, 2/1 modes have not been observed in the H-mode to date. The modes are measured only when both the stored energy and plasma rotation profiles are lowered after an H–L back-transition with q_{95} ranging from 4.3 to 6.2 ($4.9 < q_{95} < 6.4$ for 3/2 modes) and the mode evolves as q_{95} mostly increases, as shown in figure 14. Subsequent 2/1 mode locking creates a repetitive collapse of β_N by more than 50%. The existence of a triggering event and the mode onset at lower l_i expected to accompany higher bootstrap current suggests that the 3/2 mode is close to being neoclassically unstable. Figure 15 shows the 2/1 tearing mode amplitude dependence on mode rotation and local rotation shear measured by XICS [28]. A correlation is made between mode amplitude and rotation shear measured for a similar mode rotation level to decouple their effects on mode growth. The result suggests that the mode amplitude tends to be reduced with strong rotation shear. Further details on tearing mode characterization are discussed in [8].

Based on the collected information of the (2,1) island location, a discharge (shot #6272) was designed for suppression of the (2,1) mode by applying ECH/CD for suppression of the mode. ECH at 110 GHz X2 mode ECH and 170 GHz X3 mode co-ECCD were injected towards the estimated island position with power levels of ~280 kW and ~650 kW, respectively. The discharge was analysed with experimental observations and simulations. The island width and mode number were identified by Mirnov coil arrays and

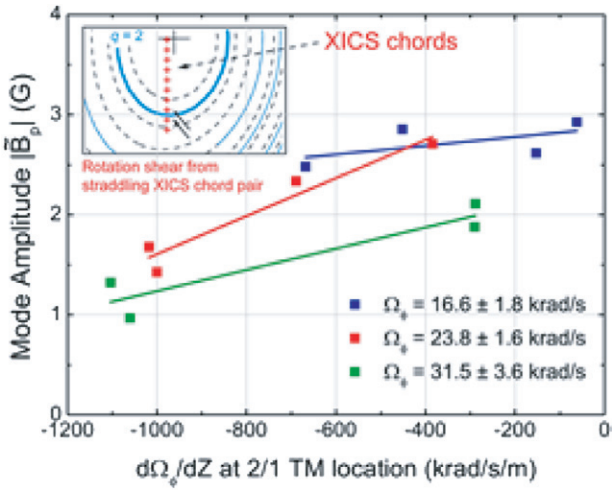

Figure 15. Mirnov amplitude for the 2/1 tearing mode versus local rotation shear from XICS.

the island location was estimated by ECE. The ECH/CD deposition was recognized by XICS. The frequency spectrum and the island width taken from Mirnov coil signals are shown in figures 16(*a*) and (*b*), respectively. As shown in figure 16, after being triggered with a small island width around 5.6 s, the tearing mode grows rapidly to the maximum island width of ∼8 cm, then gradually shrinks and terminates around 6.6 s. The mode frequency and the island width are consistent with those observed in ECE. The island radial locations are identified as $R \sim 1.5$ m (high-field side) and ∼2.05 m (low-field side) where the phase inversion of the electron temperature oscillation is shown in ECE measurements (see figure 16(*c*)). A newly developed integrated numerical system [29], coupled with the modified Rutherford equation (MRE) solver with ECH effects, was used for modelling of the mode activity by integrating plasma equilibrium, transport, heating and current drive, and magnetic island evolution, in a self-consistent way. A validation is made against another discharge (pulse 6123) with the (2,1) tearing mode where no 110 GHz X2 mode EC is used for the purpose of stabilization. The calculated island width is compared with experiment in figure 16(*d*). After validating against another discharge (pulse 6123) with the (2,1) tearing mode where no 110 GHz X2 mode EC is used for the purpose of stabilization, it was applied for modelling of the discharge (shot #6272) with TM stabilization by EC. The results are shown in figure 16(*b*) where the simulation with the EC effect is compared with that without the EC effect. It is clearly seen that the EC plays a significant role in stabilizing the tearing mode.

Intrinsic non-axisymmetry, the so-called intrinsic error field, almost always exists in tokamaks due to the imperfection of machine constructions. It is important to identify and compensate for the intrinsic error field below a threshold, since otherwise the tokamak performance can be degraded or even disrupted by locking or by unnecessary 3D neoclassical transport. The identification of the intrinsic error field is also essential to precisely understand 3D field effects such as RMP ELM suppression. In the 2011 KSTAR campaign, the investigation of the intrinsic error field was successfully initiated by applying the $n = 1$ fields to ohmic plasmas with two different toroidal phases differing by 180°. A difference in the plasma response was detected, indicating the intrinsic non-axisymmetry, and quantified by the locking threshold. With the 90 phasing configuration, the threshold was measured by $I_{\mathrm{RMP}} \sim 1.1$ kA and 1.3 kA, respectively, for each toroidal phase, as shown in figure 17. This means that the intrinsic error field corresponds to, and so can be compensated by $I_{\mathrm{RMP}} \sim 0.1$ kA. IPEC [30] calculations showed that this is equivalent to the resonant field, $\delta B_{21}/B_{\mathrm{T0}} \sim 1.5 \times 10^{-5}$. This level of asymmetry is encouragingly small, but the two different toroidal phases can provide only a partial detection of the error field, and therefore a full toroidal phase scan, separated by 90°, will be performed in the next campaign. Also, target plasmas will be extended to the fully shaped L-mode and H-mode plasmas. The measured error field threshold for locking itself is also important for locking scaling in tokamaks. We find that the locking field threshold in KSTAR is consistent with the conventional density scaling and so can be nicely combined with locking data in other devices and used for tokamak locking scaling [31].

The runaway current conversion following disruptions has an important effect on the first wall for next-generation tokamaks. Because of the potentially severe consequences of a large full current runaway beam on the first wall in an unmitigated disruption, runaway suppression is given a high priority. It is found that runaway currents can be generated following spontaneous disruptions with a toroidal magnetic field as low as $B_{\mathrm{T}} = 1.3$ T. The conversion efficiency of pre-disruption plasma current into runaway current in spontaneous disruptions is independent of the toroidal magnetic field. Runaway current generated by a spontaneous disruption can reach up to 80% of the pre-disruptive currents even at a low magnetic field. A dedicated fast valve with 40 bar high-pressure massive gas injection (MGI) has been developed for the purpose of mitigating runaway currents. The absence of runaway currents during low-Z gas shutdown has been observed in many devices [32–34], but runaway electrons were avoided by D_2 MGI only below 3 T in KSTAR, as shown in figure 18. At 3.5 T, the disruptions are prone to generate a high runaway current plateau ($I_{\mathrm{RE}}/I_{\mathrm{p}} > 70\%$) with an injection of 8.3×10^{21} D_2 molecules. This corresponds to about 83 times the plasma inventory. The generation and suppression of runaway current by D_2 MGI at $B_{\mathrm{T}} = 3.5$ T will be investigated in detail in the next campaign. This has negative implication for ITER due to its high plasma current. For ITER 15 MA operation, the amplification gain of runaways following disruption is huge (e^{50}) compared with the KSTAR experiment (e^{1}), so that the runaway generation will be more serious than previous predictions [35]. The large number of generated runaway electrons is likely to be connected with a low intrinsic error field and a low toroidal ripple field in KSTAR.

7. Alteration of toroidal rotation by ECRH and applied 3D fields

Toroidal rotation is important for control of stability and transport in tokamaks. While NBI is used widely to control rotation in contemporary tokamaks, it is not a feasible approach for ITER. Moreover, the tendency of confined tokamak plasmas to have non-zero intrinsic rotation has been identified

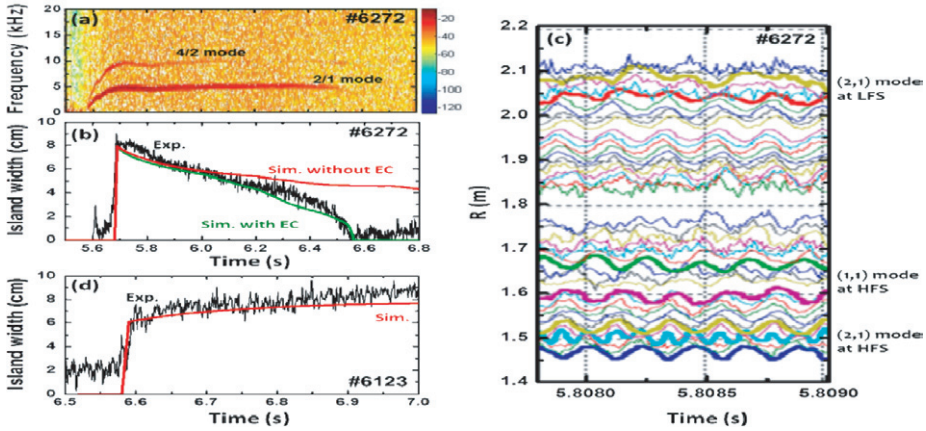

Figure 16. Time trace of (*a*) the spectrogram of a Mirnov coil signal (MC1P03), (*b*) the island width estimated from the experiment (black) and from the simulation with/without the EC effect (green/red), and (*c*) electron temperature fluctuation observed by ECE with the (2,1) tearing mode (C) in shot # 6272.

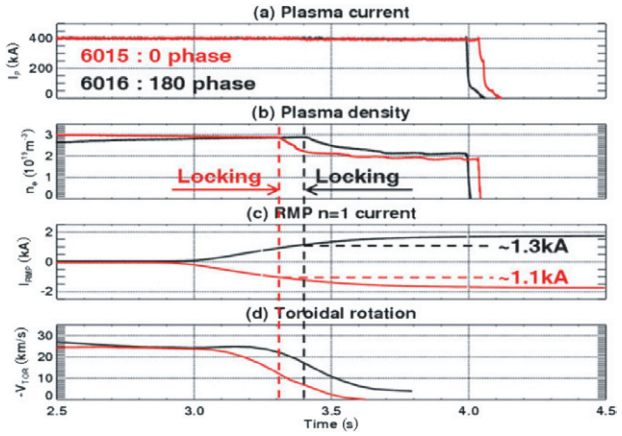

Figure 17. Plasma locking induced by $n = 1$ RMPs, with two different toroidal phases.

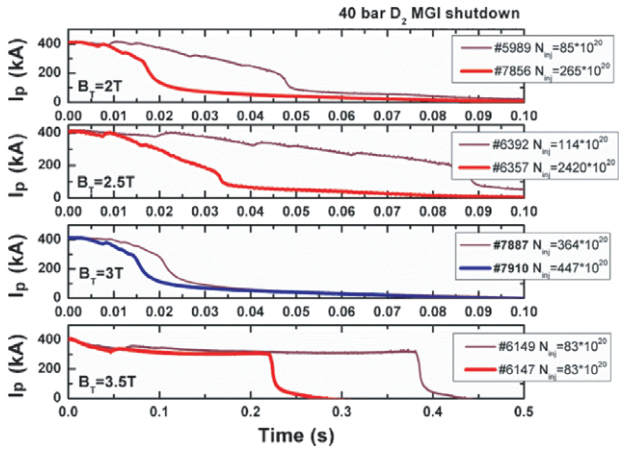

Figure 18. Time evolutions of plasma currents after D_2 MGI injection with different amounts of D_2 molecules injected at various toroidal magnetic fields. The total inventory of the target plasma is about $N_0 = 1 \times 10^{20}$. Note that the bottom plot has a different time scale.

and is related to the state of plasma confinement. Intrinsic rotation is self-generated by ambient turbulence via the non-diffusive residual stress. The residual stress can be driven by broken symmetry in the fluctuation spectrum and its sign depends on the turbulence propagation direction, which implies the reversal of intrinsic torque at the ITG $\leftrightarrow$ TEM transition [36, 37]. ECRH heating of NBI-heated discharges has been widely investigated [38–40] and 350 kW ECRH was applied to NBI-heated (1.3 MW) H-mode plasmas on KSTAR. Figure 18 shows the toroidal rotation profiles with NBI and NBI+ECRH, where the radial coordinate is defined as $\rho = \sqrt{\psi/\psi_x}$ with the poloidal magnetic flux ψ (ψ_x denotes the value at the last closed flux surface). In the core, we observed a significant drop in the toroidal rotation $\Delta V_\phi / V_\phi \sim -30\%$ and a strong correlation between ∇V_ϕ and ∇T_e (see figure 19(*b*)). Note the region of change, i.e. $\rho < \rho_{pv} \sim 0.7$ where ρ_{pv} is the point about which the profile pivots in figure 19(*a*), clearly lies within the core, not the pedestal (i.e. $\rho_{pv} < \rho_{ped}$, where ρ_{ped} is the location of the top of the pedestal). On the other hand, the pedestal rotation is unchanged. We hypothesize that the global toroidal rotation profile is determined by the interplay of (1) NBI torque (co-current direction), (2) pedestal intrinsic torque (co-current) and (3) core intrinsic torque by ECRH (counter-current) [41]. As a consequence of the T_e and V_ϕ profile changes, we found that $1/L_{T_e}$ increases, where $L_{T_e} = \frac{1}{T_e}\frac{\partial T_e}{\partial r}$, and electron collisionality decreases in the ECH deposition region, while $E \times B$ shearing changes only slightly. This suggests that there is an increased role of the fluctuation intensity gradient in the $k_\parallel$-fluctuation symmetry breaking, which is necessary for fluctuation-induced residual stress generation for intrinsic torque [36, 42, 43]. The steepened ∇T_e and reduced electron collisionality can trigger the excitation of TEM in the core. Using the gyrokinetic code GS2 [44, 45], we analysed and compared micro-instabilities before and after the ECRH injection. The profiles of V_ϕ and T_i from CES, and T_e from ECE were used. In the absence of any measured electron density profile in the 2011 campaign, based on the indirect evidence of density peaking from the argon emissivity profile, we assumed density profiles with modest peaking by ECRH. The GS2 analysis indicates that an ITG $\rightarrow$ TEM transition occurs in the deep core $\rho = 0.18$ (figure 20), which is far from the pivot point, while the ITG remains unstable with a reduced frequency and growth rate in

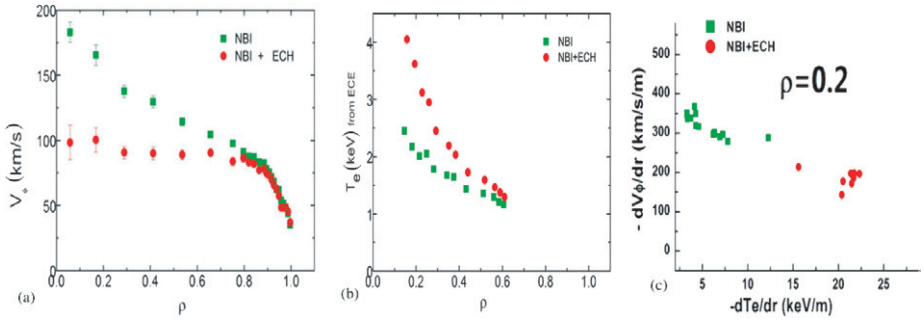

Figure 19. (*a*) Toroidal rotation (*b*) electron temperature profiles with NBI and NBI+ECH, and (*c*) correlation between ∇T_e and ∇V_ϕ at radial position $\rho = 0.2$.

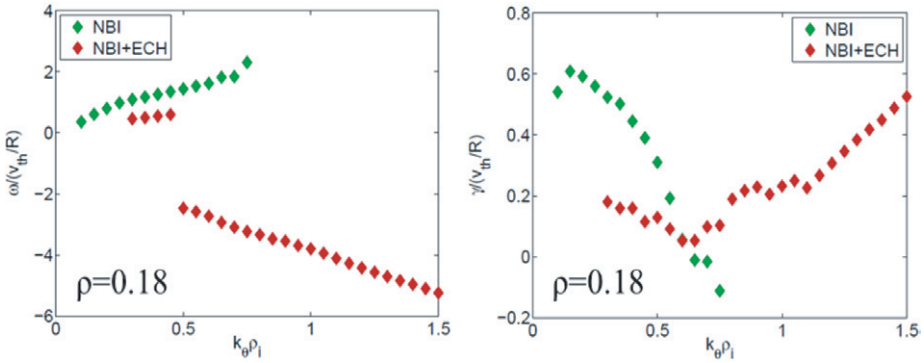

Figure 20. Comparison of the micro-instabilities before (green) and after (red) ECRH injection.

other regions. Since the analysis of micro-instabilities depends on the assumed density profile, we repeated the analysis using density profiles with different degrees of peaking. We found that the region of TEM excitation expands radially for stronger density peaking, though the radial extent of the region is still fairly limited inside the pivot point. Thus, a problem emerges, namely that the popularly favoured hypothesis is not supported by the data. To address this issue, we remark that the fluctuation intensity can spread beyond the linearly unstable region by nonlinear scattering processes such as turbulence spreading and heat avalanches [46]. Thus, resolving the physical problem may require consideration of non-locality processes. Also, the limited extent of the region, where the dominant micro-instability changes, suggests that the state of turbulence in neighbouring radial regions is very likely a dynamic, evolving mixture of ITG and TEM turbulence. A detailed study of these processes requires global nonlinear simulation and more detailed modelling, which is a subject for future work. Further experimental investigations using fluctuation diagnostics such as BES are essential to critically assess the ITG–TEM transition, which is an ongoing subject of study in the coming experimental campaigns.

On the other hand, a rotation drop with ECH injection into NBI-driven plasmas often accompanies the MHD activity such as the internal kink mode inside the $q = 1$ surface. In NBI-heated plasmas, the NTV torque density caused by the internal kink mode is comparable to the NBI torque density. Note that the ECRH-induced internal kink modes were generally accompanied by sawtooth oscillations since the safety factor q decreases below one in the core region with the appearance of the $m = 1$, $n = 1$ mode. The magnitude of the toroidal rotation velocity is reduced by electron ECRH regardless of the direction of toroidal rotation [47]. As shown in figure 21(*a*), the core toroidal rotation was reduced in the NBI-heated plasmas rotating in the co-current direction when ECRH was injected in the core and recovered when ECRH was turned off. On the other hand, the toroidal rotation speed changed in the co-current direction when ECRH was injected in the ohmic-heated plasmas rotating in the counter-current direction, as in figure 21(*b*). It was found that central ECRH induces the internal kink mode inside the $q = 1$ surface. The magnetic field perturbation driven by the internal kink mode enhances the neoclassical toroidal plasma viscosity, which is otherwise assumed to be negligible. Thus, the toroidal rotation can be damped by the enhanced toroidal viscosity. The MHD-activity-induced toroidal viscosity was introduced in [48] and the NTV theory in each collisionality regime has been developed recently. The NTV damps the toroidal rotation towards the steady-state toroidal flow, which is generally in the counter-current direction. When the torque density is present, the toroidal rotation profile attains a steady state when the NTV torque is balanced with other torque sources and sinks. In [47], the NTV torque density is estimated from the magnetic field perturbation, δB. In NBI-heated plasmas, the NTV torque density caused by the internal kink mode is comparable to the NBI torque density for the steady-state toroidal rotation profile. It seems that the internal kink mode driven by ECRH is due to interactions between energetic electrons generated by ECRH and an $m = 1, n = 1$ mode. The internal kink modes appeared only when the ECRH was turned on. In ignition tokamaks such as ITER, the alpha particles generated by fusion reactions will transfer their energy to the electrons by collisions. Then, the

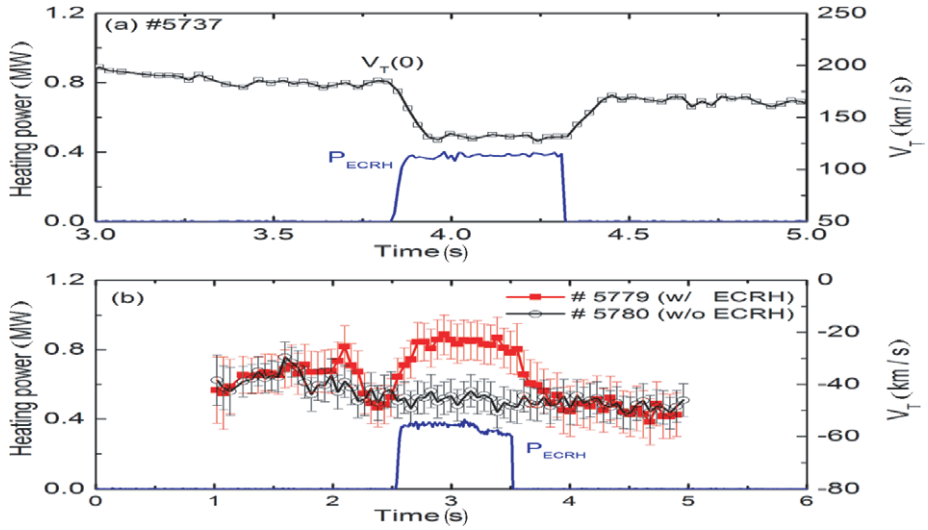

Figure 21. (*a*) The time trace of the core toroidal rotation speed for shot 5737 measured by XICS. $R = 1.81$ m, $a = 0.48$ m, $\kappa = 1.81$, $q_{95} = 6.5$, $I_p = 0.6$ MA, $B_T = 1.96$ T. (*b*) The time traces of the core toroidal rotation speed for ohmic heated discharges with (square) and without (circle) ECRH, measured by XICS. On-axis ECRH at 400 kW was injected at $t = 2.5$–3.5 s for shot 5779. $R = 1.8$ m, $a = 0.5$ m, $\kappa = 1.15$, $q_{95} = 6.0$, $I_p = 0.3$ MA, $B_T = 1.96$ T.

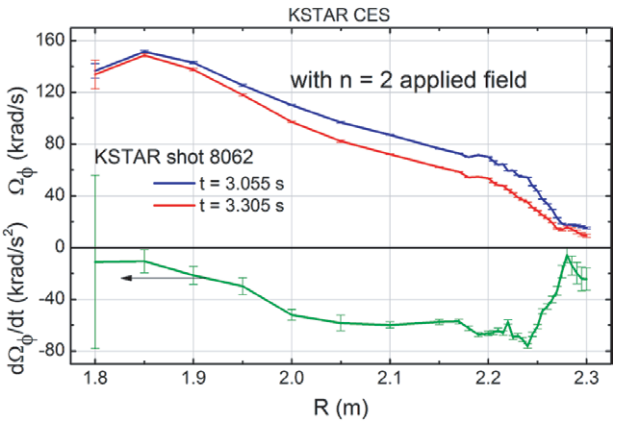

Figure 22. Net rotation profile change by an $n = 2$ applied field in the H-mode rotation profile.

internal kink modes driven by energetic electrons, may appear and reduce the toroidal rotation in the core region of the ignition tokamaks.

The plasma rotation is also changed by non-axisymmetric magnetic fields. This is an important tool for rotation control in mono-directed NBI-heated tokamak plasmas, to reduce plasma rotation into ITER-relevant ranges, and to study the underlying NTV physics [5, 48, 49]. Success in non-resonant alteration of the plasma rotation profile by applied $n = 1$ and 2 fields was obtained. Figure 22 illustrates the variation of the plasma toroidal rotation profile during the H-mode operation using an $n = 2$ applied field generated by IVCC. Plasma boundary movement was properly compensated in the calculation of the rotation profile change measured by CES [50]. The profile rotation difference shown occurs as the $n = 2$ IVCC field rises to a steady-state value in several tens of milliseconds, and therefore is predominantly due to this applied field. The typical slow decrease in rotation due to a longer (several seconds) timescale plasma density increase is significantly less than the rotation reduction caused by the applied $n = 2$ field. The experiment was reproduced at several levels of initial rotation by stepping the applied $n = 2$ field magnitude. Analysis of existing data shows that saturated $n = 1$ and 2 rotating mode activity potentially leading to resonant rotation damping only appears in the plasma core, and so is absent from the observed region where applied $n = 2$ field-related braking is strongest. In addition, this saturated rotating mode activity appears continuously in the discharge, and therefore its saturated effect on the rotation profile is eliminated in the analysis shown in figure 22. In addition, pedestal rotation profiles were measured during ELM suppression experiments using an $n = 1$ RMP. We obtained an ELM-mitigated state by applying $n = 1$ RMP with coil current $I_c = 1.8\,\mathrm{kA\,t^{-1}}$ and a zero phasing configuration. Figure 23 unambiguously shows that the V_ϕ pedestal top value drops during ELM mitigation. The rotation pedestal width also expands during the duration of ELM mitigation, as shown in figure 23 [51]. Generally, V_ϕ decreases during ELM mitigation but recovers its pre-mitigation value once ELMs reappear.

8. Wall conditioning using RF plasmas and dust in the vessel

During the last four years of operation, vacuum venting occurred many times due to accidents. In order to recover the wall condition to access the H-mode, the vacuum vessel and PFCs were initially baked up to 130 °C. After the baking process, the levels of impurity partial pressures were reduced down to $\sim 1 \times 10^{-9}$ mbar, and the wall condition recovered. Although the main cleaning is performed by GDC, wall conditioning techniques in the presence of a permanent magnetic field are one of the major topics of the plasma–surface interaction (PSI) program in KSTAR: ion cyclotron wall conditioning (ICWC) and electron cyclotron wall conditioning (ECWC) [52, 53]. Two main experimental goals of ICWC in the 2011 campaign were to (1) increase the poloidal homogeneity by applying a vertical magnetic

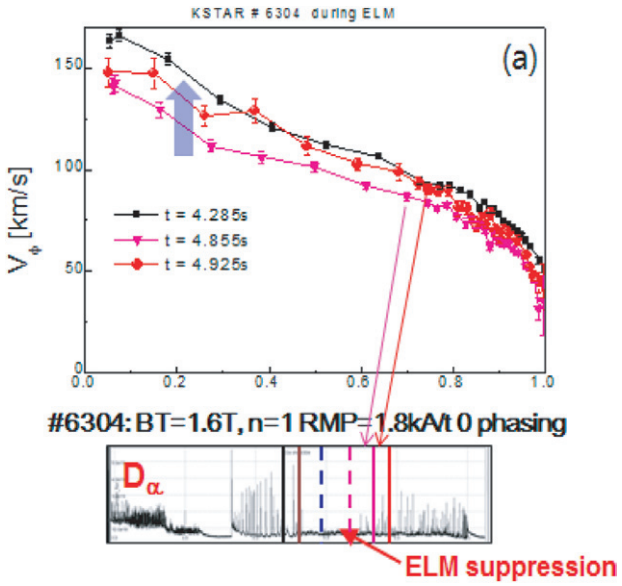

Figure 23. Toroidal rotation evolution during ELM mitigation by RMP. The magenta colour shows the mitigated ELM case.

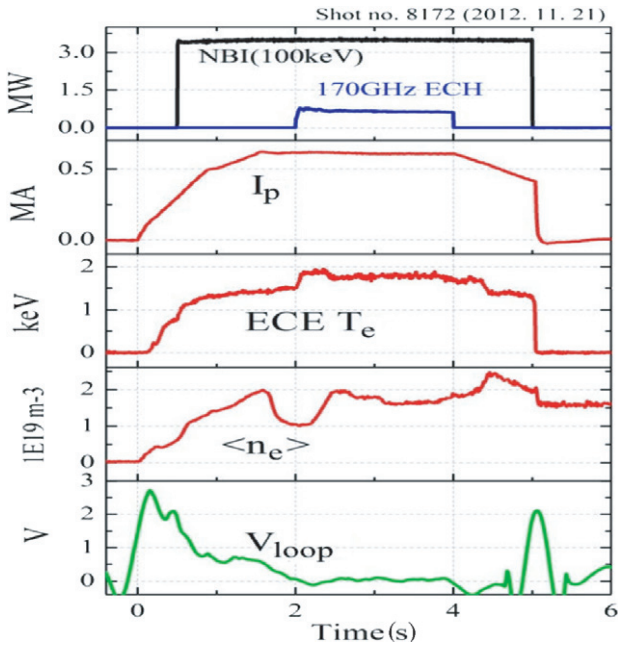

Figure 24. Full power operation of NBI with 3.5 MW at 100 keV of beam energy (shot #8172).

field, B_v, (2) increase the plasma wetted area (thus, cleaning efficiency). For a small B_v (<0.05 T), an ICWC plasma is located at the out-board side. As B_v increases to ~0.1 T, the ICWC plasma starts to expand towards the in-board side, and finally reaches the divertor, where the plasma is fully expanded to the in-board side. As B_v increases further, the ICWC plasma moves upwards. The fundamental ECRF heating at 110 GHz was applied at the position of $B_T = 3.94$ T with a helium gas pressure of $\sim 5 \times 10^{-3}$ mbar and an additional horizontal magnetic field, $B_H = 0.02$ T. The ECWC plasmas were not as uniform as those in JT-60U, the ECWC plasmas were extended in the radial direction and high-density plasmas with densities up to 2.3×10^{19} m^{-3} were produced. It was found that the injection angle of an ECRF wave was not essential for the fundamental ECRF heating. Finally, ECWC was applied for disruption recovery, and demonstrated that a reference tokamak discharge was successfully generated.

The characteristics and behaviour of in-vessel dusts are analysed by CCD image processing techniques. These techniques allow us to get information on the temporal evolution of dust creation events (DCEs), most probable origins and the velocity distribution. It is found that the dust creation origins are strongly dependent on the plasma–surface interaction and the history of the plasma scenarios. In diverted plasma operation, DCEs were observed mainly in the divertor region, while DCEs were observed randomly in the vacuum vessel with a limiter configuration. The velocity range of detected dust particles was from 7 to 385 m s^{-1} with a peak at 30 m s^{-1} in the 2010 campaign and from 9 to 417 m s^{-1} with a peak at 50 m s^{-1} in the 2011 campaign. The dust velocity is increased with an increase in input power. Note that much faster dust velocities can exist but they cannot be detected due to the limits of detection of the CCD camera.

9. Heating and the current drive system

The NBI system is the main actuator for both heating and current drive in KSTAR. Therefore, an enormous amount of effort has been made for development of the NBI system from the start of the KSTAR project. As a result, the first commissioning of the NBI using positive ions was completed prior to the 2010 campaign. The maximum NB power was estimated to be more than 1.2 MW for a beam energy of 90 keV. The transport efficiency was estimated to be about 78% with beam perveance in the range 1.25–1.3 μ-P. The first ion source was completed through a combination of a plasma source chamber developed by JAEA within the framework of the KO-JA fusion collaboration and an accelerator developed by KAERI. A longer pulse beam extraction was also demonstrated in 2011 and a 300 s duration beam at 80 keV was achieved [54]. For the NB system upgrade in 2012, the second ion source, which was developed by KAERI, and the associated power supplies and beam line components were newly installed. The upgraded NBI system was stably operated in the 2012 campaign with more than 3 MW of NB for a 20 s in maximum pulse length at 90 keV of beam energy. As shown in figure 24, the NBI also demonstrated a power of 3.5 MW NB injection to the plasma at 100 keV of beam energy for 5 s at the end of the 2012 campaign.

The electron cyclotron heating and current drive (EC H&CD) system operating at a frequency of 170 GHz was developed for the control of the local plasma current profile to affect internal MHD such as the neoclassical tearing mode (NTM) critical in high-beta plasma operation. The initial 170 GHz, 1 MW EC H&CD system was successfully commissioned and used for the second-harmonic ECH-assisted startup in the 2011 operational campaign of the KSTAR [55]. Because reducing the flux consumption could also reduce the flux burden of superconducting machines such as ITER, it is one of the critical issues in ITER. Using the same gyrotron frequency as planned for ITER, assisted start-up was performed in KSTAR with an EC beam power of

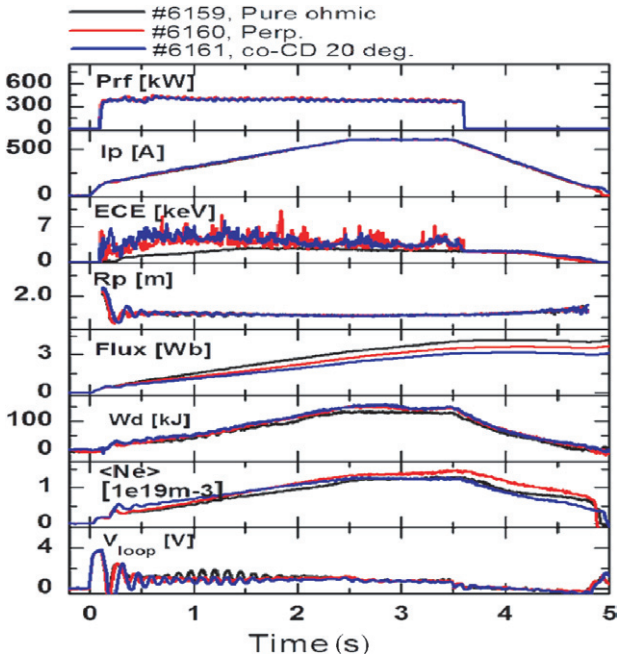

Figure 25. Time evolution of flux consumption for various ECH heating scenarios.

0.4 MW launched from the low-field side. A second harmonic EC-assisted plasma startup was compared with KSTAR pure ohmic start-up, which is defined as a discharge without ECH during the start-up. Beginning at 100 ms after the initial breakdown, all KSTAR poloidal field coils are feedback-controlled to maintain a pre-programmed plasma current and plasma position at $R = 1.8$ m. The time evolution of the applied power and the main parameters together with the ohmic consumption are shown in figure 25. For the pure ohmic start-up as a reference shot 6159, the loop voltage at the breakdown was ∼3.7 V and the flux consumption up to the start of the current flattop was ∼4.13 Wb. For the ECH-assisted start-up with X2 perpendicular injection, the flux consumption at the start of the current flat-top was reduced to $\Delta\Phi \sim 3.62$ Wb and more reduction in the magnetic flux consumption was obtained with $\Delta\Phi \sim 3.14$ Wb when the EC beam was launched with a toroidal angle of 20° in the co-CD direction.

A 5 GHz lower hybrid current drive (LHCD) system has been developed for the past several years [56] with the help of collaboration between CEA-IFRM in France and MIT in the US. A 0.3 MW/2 s LHCD system was completed in the middle of 2012, which was followed by an initial operation in the 2012 campaign. The launcher of the LHCD system is a fully active waveguide grill with an array of eight waveguides in columns and four waveguides in rows based on a four-way splitter without active water cooling. The 5 GHz klystron finally demonstrated 500 kW at 600 s of pulse length, which confirms successful development of the 5 GHz klystron with 500 kW for steady-state operation. In spite of the best results in the klystron commissioning, the limited capability of the launcher for power handling, and an insufficient number of key components for system safety such as circulators were a major concern for the initial LHCD operation. Therefore, more efforts should be made to optimize the initial 5 GHz LHCD system for the 2013 campaign.

10. Summary and future plans

Since the first H-mode discharge in 2010, H-mode has been sustained longer and the operational regime of plasma parameters has been significantly extended. L–H transitions were obtained with 0.8–3.0 MW of NBI in single- or double-null configurations and the H-mode lasted up to ∼15 s at 0.6 MA of plasma current. The measured power threshold as a function of density showed a roll-over with a minimum value of ∼0.8 MW at $\bar{n}_e \sim 2 \times 10^{19}$ m^{-3}. Based on the achievement of a high-beta H-mode, various methods of ELM control were implemented including RMP, SMBI, vertical jogging and ECCD injection on the pedestal. We observed various ELM responses, i.e. suppression and mitigation, depending on the relative phases of the IVC coils. In particular, ELMs were completely suppressed by the 90° phase of the $n = 1$ RMP, and the IPEC and NTV analyses showed that the +90 phase RMP indeed can give the largest Chirikov overlap width in the edge and the smallest NTV torque in the core, compared with other RMP configurations. ELM pace-making by fast vertical jogging of the plasma column was also demonstrated. A state of mitigated ELMs for a few tens of ELM periods was sustained by the optimized repetitive SMBI pulses. The ECE-I diagnostic visualized the ELM dynamics in 2D during the mitigation and suppression processes. In addition to the ELM control experiments mentioned above, the observed rotation drop by ECRH in NB-heated plasmas was investigated in terms of either a reversal of the turbulence-driven residual stress or changes in the NTV torque by the internal kink mode. The suppression of the runaway electrons using MGI of deuterium showed that runaway electrons were avoided only below 3 T in KSTAR. An experiment for stabilization of the (2,1) tearing mode by ECH/CD has been conducted in which the effect of EC was evaluated by integrated modelling. It is the first step towards real-time feedback control of NTM in KSTAR, a high priority task in preparation for ITER.

In the 2012 campaign, we reached and surpassed the $n = 1$ ideal MHD no-wall stability boundary with doubled NBI power, and improved iso-flux plasma control. Normalized beta has reached 2.9, and β_N/l_i has exceeded 4. Operation in 2013 is expected to exceed the $n = 1$ ideal MHD no-wall stability boundary more routinely. Therefore, resistive wall modes can be expected, motivating active $n = 1$ RWM control experiments. From an engineering viewpoint, utilization of the motor generator will make the full ohmic flux swing possible in 2013, and an upgrade of the total heating power up to 15 MW by 2015 will lead to the completion of commissioning of tokamak performance such as $I_p = 2$ MA long-pulse operation. So the next five years will be a challenging and interesting working period for KSTAR because it can provide long-pulse/high-performance plasmas for its original aim. However, in consideration of the efficient utilization of human and hardware resources, it is necessary for both KSTAR and Korean fusion researchers to develop their specific/intrinsic research items in line with the KSTAR mission for fusion energy development in Korea. A full tungsten wall would be one of the candidate programmes. In addition, it is strongly recommended for

KSTAR to focus its research direction on ITER-relevant urgent issues such as ELM control, 3D physics and disruption prediction, avoidance and mitigation in order to contribute to ITER within the framework of ITPA. To accomplish this goal, a total heating resource upgrade up to 15 MW with more reliable basic diagnostics is strongly required and the pellet injector would be one of the essential tools to support physics programme. In addition, strong collaboration with domestic and foreign collaborators is urgently needed to reinforce the human resources needed to produce the fusion science in KSTAR.

Acknowledgments

This work was supported by the Ministry of Education, Science and Technology of Korea. The KSTAR Team is grateful to the domestic and international collaboration partners for their support with various research activities.

References

[1] Kim K. *et al* 2012 A preliminary conceptual design study for korean fusion DEMO reactor *Fusion Eng. Des.* (Special issue for the SOFT 2012 conference) submitted
[2] Kwon M. *et al* 2011 *Nucl. Fusion* **51** 09
[3] Yoon S.W. *et al* 2011 *Nucl. Fusion* **51** 113009
[4] Katsuro-Hopkins O. *et al* 2010 *Nucl. Fusion* **50** 025019
[5] Sabbagh S.A. *et al* 2010 *Nucl. Fusion* **50** 025020
[6] Berkery J.W. *et al* 2010 *Phys. Plasmas* **17** 082504
[7] Sabbagh S.A. *et al* 2006 *Nucl. Fusion* **46** 635
[8] Park Y.S. *et al* 2012 *Proc. 24th Int. Conf. on Fusion Energy (San Diego, CA, 2012)* (Vienna: IAEA) paper EX/P2-07 and www-web.iaea.org/napc/physics/FEC/FEC2012/papers/140_EXP207.pdf *Nucl. Fusion* submitted
[9] Degeling A.W. *et al* 2003 *Plasma Phys. Control. Fusion* **45** 1637
[10] Park H. *et al* 2012 *Proc. 24th Fusion Energy Conf. (San Diego, CA, 2012)* (Vienna: IAEA) EX11-3
[11] Ahn J.-W. *et al* 2012 *Nucl. Fusion* **52** 114001
[12] Kim H.S. *et al* 2012 *Proc. 24th Fusion Energy Conf. (San Diego, CA, 2012)* (Vienna: IAEA) EX/P7-19
[13] Kim J. *et al* 2012 *Nucl. Fusion* **52** 114011
[14] Evans T.E. 2004 *Phys. Rev. Lett.* **92** 235003
[15] Yao L.H. *et al* 2002 *Proc. 19th Int. Conf. on Fusion Energy 2002 (Lyon, France, 2002)* (Vienna: IAEA) CD-ROM file EX/P4-08 and www.iaea.org/programmes/ripc/physics/fec2002/html/fec2002.htm
[16] Jeon Y.M. *et al* 2012 *Phys. Rev. Lett.* **109** 035004
[17] Park J.K., Boozer A.H. and Menard J.E. 2009 *Phys. Rev. Lett.* **102** 065002
[18] Fenstermacher M.E. *et al* 2008 *Phys. Plasmas* **15** 056122
[19] Yiang Y. *et al* 2007 *Phys. Rev. Lett.* **98** 265004
[20] Xiao W.W. *et al* 2012 *Nucl. Fusion* **52** 114027
[21] Nam Y.U. *et al* 2012 *Rev. Sci. Instrum.* **83** 10D531
[22] Xiao W.W. *et al* 2013 *Nucl. Fusion* submitted
[23] Gruzinov I., Diamond P.H. and Rosenbluth M.N. 2002 *Phys. Rev. Lett.* **89** 25
[24] Gruzinov I., Diamond P.H. and Rosenbluth M.N. 2002 *Phys. Plasmas* **10** 569
[25] Rhee T. *et al* 2012 *Phys. Plasmas* **19** 022505
[26] Kogi Y. *et al* 2008 *Rev. Sci. Instrum.* **79** 10F115
[27] Yun G.S. *et al* 2010 *Rev. Sci. Instrum.* **81** 10D930
[28] Lee S.G. *et al* 2010 *Rev. Sci. Instrum.* **81** 10E506
[29] Kim K. 2013 Feedback control of neoclassical tearing mode in time-dependent simulation on tokamak plasmas *Nucl. Fusion* submitted
[30] Park J.K. *et al* 2007 *Phys. Plasmas* **14** 052110
[31] Menard J.E. *et al* 2010 The study of the error fields using Ideal Perturbed Equilibrium Code (IPEC) *ITER Task Agreement* #C19TD22FU
[32] Finken K.H. 2001 *Nucl. Fusion* **41** 1651
[33] Hender T.C. *et al* 2007 Progress in the ITER Physics Basis: chapter 3. MHD stability, operational limits and disruptions 2007 *Nucl. Fusion* **47** S128–202
[34] Bozhenkov S.A. *et al* 2008 *Plasma Phys. Control. Fusion* **50** 105007
[35] Putvinskiy S. 1997 *Plasma Phys. Control. Fusion* **39** B157–71
[36] Diamond P.H. *et al* 2008 *Phys. Plasmas* **15** 012303
[37] Rice J.E. *et al* 2011 *Phys. Rev. Lett.* **107** 265001
[38] McDermott R.M. *et al* 2011 *Plasma Phys. Control. Fusion* **53** 035007
[39] DeGrassie J.S. *et al* 2007 *Phys. Plasmas* **14** 056115
[40] Sakamoto Y. *et al* 2006 *Plasma Phys. Control. Fusion* **48** A63
[41] Shi Y. *et al* 2013 *Proc. 24th Fusion Energy Conf. (San Diego, CA, 2012)* (Vienna: IAEA) EX/2-3 *Nucl. Fusion* submitted
[42] Diamond P.H. *et al* 2009 *Nucl. Fusion* **49** 045002
[43] Gurcan O.D. *et al* 2007 *Phys. Plasmas* **14** 042306
[44] Kotschenreuther M., Rewoldt G. and Tang W.M. 1995 *Comput. Phys. Commun.* **88** 128
[45] Dorland W., Jenko F., Kotschenreuther M. and Rogers B.N. 2000 *Phys. Rev. Lett.* **85** 5579
[46] Gurcan O.D. *et al* 2005 *Phys. Plasmas* **12** 032303
[47] Seol J. *et al* 2012 *Phys. Rev. Lett.* **109** 195003
[48] Shaing K.C. *et al* 2003 *Phys. Plasmas* **10** 1443
[49] Zhu W. *et al* 2006 *Phys. Rev. Lett.* **96** 225002
[50] Ko W.H. *et al* 2010 *Rev. Sci. Instrum.* **81** 10D740
[51] Ko W.H. *et al* 2012 *Proc. 24th Fusion Energy Conf. (San Diego, CA, 2012)* (Vienna: IAEA) PD/P8-22
[52] Lyssoivan A. 2012 *Plasma Phys. Control. Fusion* **54** 074014
[53] Itami K.J. 2009 *Nucl. Mater.* **390–391** 983
[54] Bae Y.S. *et al* 2012 *Fusion Eng. Des.* **87** 1597
[55] Jeong J.H. *et al* 2012 Commissioning of 170 GHz, 1 MW EC H&CD in KSTAR *17th Joint Workshop on Electron Cyclotron Emission and Electron Cyclotron Resonance Heating* vol 32, 02019
[56] Park S. *et al* 2010 *Fusion Eng. Des.* **85** 197